Superfluid response of two-dimensional filamentary superconductors

Giulia Venditti[1,8 †*], Ilaria Maccari[2, 9 †], Alexis Jouan[3], Gyanendra Singh[3,4], Ramesh C. Budhani[5], Cheryl Feuillet-Palma[3], Jérôme Lesueur[3], Nicolas Bergeal[3], Sergio Caprara[6,7*], and Marco Grilli[6,7*]

1 SPIN-CNR Institute for Superconducting and other Innovative Materials and Devices, Area della Ricerca di Tor Vergata, Via del Fosso del Cavaliere 100, 00133 Rome, Italy
2 Department of Physics, Stockholm University, Stockholm SE-10691, Sweden
3 Laboratoire de Physique et d'Étude des Matériaux, ESPCI Paris, PSL University, CNRS, Sorbonne Université, Paris, France
4 Institut de Ciéncia de Materials de Barcelona (ICMAB-CSIC), Campus de la UAB, 08193 Bellaterra, Catalonia, Spain
5 Department of Physics, Morgan State University, Baltimore, Maryland 21210, USA
6 Dipartimento di Fisica, Università di Roma "Sapienza", P.le Aldo Moro 5, I-00185 Roma, Italy
7 CNR-ISC, via dei Taurini 19, I-00185 Roma, Italy
8 Present address: DQMP, University of Geneva, 24 Quai Ernest-Ansermet, CH-1211 Geneva, Switzerland
9 Present address: Laboratory for Theoretical and Computational Physics, Paul Scherrer Institute, 5232 Villigen PSI, Switzerland
[†] These authors contributed equally.
[*] giulia.venditti@unige.ch   marco.grilli@roma1.infn.it   sergio.caprara@roma1.infn.it

October 20, 2023

Abstract

Different classes of low-dimensional superconducting systems exhibit an inhomogeneous filamentary superconducting condensate whose macroscopic coherence still needs to be fully investigated and understood. Here we present a thorough analysis of the superfluid response of a prototypical filamentary superconductor embedded in a two-dimensional metallic matrix. By mapping the system into an exactly solvable random impedance network, we show how the dissipative (reactive) response of the system non-trivially depends on both the macroscopic and microscopic characteristics of the metallic (superconducting) fraction. We compare our calculations with resonant-microwave transport measurements performed on $LaAlO_3/SrTiO_3$ heterostructures over an extended range of temperatures and carrier densities finding that the filamentary character of superconductivity accounts for unusual peculiar features of the experimental data.

1 Introduction

The availability of low-dimensional compounds exhibiting superconductivity is steadily increasing, often displaying unconventional behaviours in their physical properties. The unavoidable presence of (even weak) microscopic disorder in the vast majority of two-dimensional (2D) materials, as well as other external and/or internal electronic interactions, can fragment the SC condensate leading to inhomogeneity on a mesoscopic scale. In particular, there is increasing evidence that in several classes of low-dimensional superconducting (SC) systems the strongly inhomogeneous nature of the electronic condensate appears as a filamentary SC pattern. Inhomogeneous superconductivity can indeed result from several different mechanisms, where the competition of the SC order parameter with other phases can act as a primary source of filamentarity. This is the case for the competition with charge-density waves in high-temperature SC cuprates [1,2], in Cu-intercalated TiSe$_2$ [3,4] and in HfTe$_3$ [5]. Hints of filamentary superconductivity have been observed also in the low-temperature antiferromagnetic phase of Fe-based superconductors [6–11], persisting until the long-range antiferromagnetic order is completely suppressed. The clustering of superconducting electrons into anisotropic stripe-like or puddle-like geometry is found also in WO$_{2.90}$ probably caused by the presence of W^{5+} - W^{5+} electron bipolarons [12]. Alongside chemical doping, also gating fields can trigger phase separation leading to a filamentary SC condensate. For instance, the ion-liquid gating technique, used to inject and tune the number of carriers in systems such as transition metal dichalcogenides (TMD) and transition metal nitride (TMN), can induce a negative compressibility while acting as a primary source of phase separation [13]. One paradigmatic class of materials displaying a strong anisotropy of superconducting regions in their two-dimensional electron gas (2DEG) are SrTiO$_3$-based heterostructures, like, e.g., LaAlO$_3$/SrTiO$_3$ (LAO/STO). The inhomogeneities in these systems can be ascribed to various causes related to oxygen vacancies [14,15], to the so-called *polar catastrophe* caused by the abrupt polar discontinuity between stacked planes [16,17], to a kind of combination of them [18] or to the sizable Rashba spin-orbit coupling [19,20].

While the microscopic origin of filamentary superconductivity depends on the specific nature of the system under investigation, some properties of the emergent SC condensate are generically related to its filamentary inhomogeneous nature, the study of which is therefore of interest to a very broad class of systems. Indeed, it has already been discussed how the anomalous transport properties observed in some inhomogeneous superconductors can be almost entirely ascribed to spatial inhomogeneities of the condensate on a mesoscopic scale rather than to its microscopic nature. That is the case, for instance, of the large broadening of the resistive transition, which cannot be ascribed to paraconductivity effects [21], but is instead the hallmark of the percolating nature of the SC transition. Furthermore, the relative width of the transition $\Delta T_c/T_c = (T_h - T_c)/T_c$, where T_h is the temperature of the first high-temperature-downturn of R and T_c is the zero-resistance temperature, gives a *quantitative measure* of the inhomogeneity of the sample. In fact, paraconductivity effects due to Cooper pair fluctuations, e.g., *à la* Aslamazov-Larkin or *à la* Halperin-Nelson, can account at most for widths of the transition of the order $\Delta T_c/T_c \sim 0.1$, whereas in several compounds such as STO-based heterostructures [21–23], TMD [4, 24], TMN [13, 25] one observes $\Delta T_c/T_c \sim 1$. Along with the broad resistive transition, anomalous metallic states, sometimes termed 'failed superconductors', also find an explanation in this percolative transition scenario, which we proposed inspired by the seminal work of Kirkpatrick [26]. This is the case, for instance, of granular and amorphous films of TaN_x and InO_x [27, 28]. Failed superconducting behaviours are also found in films of Bi, Al, In, Ga, Pg, Sn, and $a-MoGe$ (see [29] for a review). More recently, a similar theoretical framework was also used to account for the anomalous transport properties observed in random nanocrystalline samples fabricated combining half-metallic ferromagnet and SC components [30]. Likewise, the observation on non-linear IV characterics [31] or pseudo-gap signatures in the tunneling spectra of STO-based interfaces [32] at temperatures higher than T_c have also been connected with the physics of inhomogeneities. Finally, the well-known conundrum of pre-forming Cooper pairs in the pseudogap region of cuprates has been related to a possible percolative scenario emerging from the presence of strong inhomogeneities [33, 34]. Yet, the debate is still ongoing [35].

So far several studies have focused on the effect of the mesoscale inhomogeneity on the SC transition above the critical temperature, while few studies have investigated the superfluid response of the resulting filamentary condensate [36, 37]. In this paper, we face this issue by mapping the problem into a random-impedance network (RIN) model that we solve exactly. By studying different RIN realizations, we show how the superfluid response of the system non-trivially depends on its microscopic and macroscopic characteristics. At the same time, by comparing our theoretical results with complex conductivity measurements on $LaAlO_3/SrTiO_3$ (LAO/STO) interfaces, we show how the different doping regimes can be understood in terms of an intrinsically less or more robust filamentary SC condensate.

The paper is organized as follows. In Section 2, we introduce the problem of the superfluid stiffness in a filamentary superconductor. In Section 3, we discuss the RIN model implemented to study the odd features that can arise from a fractal-like geometry of the superconducting condensate. Sections 4 and 4.1 are devoted to the specific case of $LaAlO_3/SrTiO_3$ (LAO/STO) interfaces, summarizing what has been done and what are the unconventional observations of superfluid density and residual conductivity. Finally, in Section 5 we present our theoretical results and in Section 6 our conclusions.

2 Filamentary superconductivity

Disregarding the specific microscopic origin of inhomogeneities, we aim at investigating the superfluid stiffness response of a filamentary superconductor.

According to the Bardeen-Cooper-Schrieffer (BCS) theory, in conventional superconductors the energy scale Δ – associated with the formation of the Cooper pairs – is much smaller than the superfluid stiffness J_s – associated with the global phase rigidity of the SC condensate. Being $\Delta \ll J_s$, the superconducting transition is thus essentially driven by the suppression of Δ. This scenario holds even in the presence of strong disorder and partially inhomogeneous systems [38, 39]. At the same time, in BCS conventional superconductors, $J_s \approx E_F$ (E_F being the Fermi energy of the metal) is directly proportional to the number of superfluid carriers n_s, with $J_s \sim n_s/m^*$, and m^* the effective carrier mass. Due to this proportionality, J_s and n_s are often used synonymously. However, it is important to emphasize here that superfluid density and superfluid stiffness are generally two separate quantities. That is clear in those SC systems where, being $J_s < \Delta$, the SC phase transition is driven by phase fluctuations that destroy the phase rigidity of the condensate while preserving a finite density of paired carriers. Granular superconductors and some Josephson-junction arrays are well-known examples of such cases. In 2D superconductors, the leading role of phase fluctuation emerges clearly in the Berezinskii-Kosterlitz-Thouless (BKT) theory [40–42] that provides a clear picture of the SC transition in terms of vortex-antivortex binding [39]. The BKT fingerprints in real SC systems can be, however, partially or completely masked by the presence of disorder. While spatially uncorrelated disorder is essentially irrelevant to the BKT SC transition [43, 44], the presence of spatially-correlated inhomogeneities can, indeed, significantly modify its nonuniversal properties [45, 46]. Finally, in some systems, the inhomogeneities are so strong and correlated in space, that the vortex-antivortex unbinding is no longer the leading mechanism for the SC transition [31]. An even stronger role of phase fluctuations takes place in quasi-one-dimensional superconductors, where the so-called phase slips, induced either by thermal or quantum excitations, prevent the onset of a global SC phase coherence [47].

The occurrence of superconductivity on structures made of random nearly 1D filaments, which can intersect and/or go almost parallel, obviously raises the complex issue of phase rigidity both at the local level of single filaments and at the global level of interconnected filaments with more or less pronounced long-range connectivity. While this issue was already addressed some time ago for DC transport [48], and in comparing the BKT physics with the effects of inhomogeneities [31], it is of obvious interest to directly investigate, both experimentally and theoretically, the phase rigidity of the condensate in such complex filamentary geometry. In the present work, we precisely aim at studying the superfluid response of a filamentary superconductor, devoting specific attention to the separate role of local and global (geometric) properties and their specific role in determining the complex conductivity response.

Having this goal in mind, we investigate a model system, keeping separate the role of the geometric structure, i.e., the density of filaments and their long-range connectivity, and the role of local disorder, from the role of local superfluid density and conductivity. The former determines the distribution of the local superconducting temperature in the various regions of the system (embedded in an otherwise metallic matrix), while the latter the local stiffness in the single individual pieces of the random superconducting structure.

To keep our study as general as possible, we will assume the filamentary structure to be given from the start, regardless of its microscopic origin.

3 Theoretical description: the Random Impedance Network

Several 2D superconducting systems, such as LAO/STO [48, 49], TMD, and TMN [13], exhibit an unusual gradual and broad vanishing of $R(T)$ that cannot be ascribed to conventional SC fluctuations but rather to the emergence of an inhomogeneous SC condensate. The first depletion of $R(T)$ by lowering the temperature can be, indeed, attributed to the appearance of

SC puddles, i.e., rather bulky regions that, at lower temperatures, get connected through SC filamentary branches, with long-distance connectivity, ultimately responsible for the long tail of $R(T)$ approaching the critical temperature (see Fig. 1). In what follows, we will refer to the bulky SC puddles with the subscript (b), and to the filamentary SC regions with (f).

In a series of previous works, we demonstrated that DC transport in such strongly inhomogeneous compounds can be conveniently described by a Random Resistor Network (RRN) model [26], in which the 2D system is discretized on a square lattice, where each bond is associated with a resistor. Kirchhoff's and Omh's Law's are then exactly solved for all currents and voltages on bonds and nodes, given an applied external voltage V^{ext} and open boundary conditions. More details about the algorithm can be found in Appendix A.
Note that in this *coarse graining* procedure, a resistor represents a *mesoscopic* region, large enough so that a critical temperature can be locally defined, but small enough with respect to the size of the sample.

While part of the resistors remains in the normal-metal state down to the lowest attained temperatures, thereby forming a metallic matrix, some others become superconducting when T decreases below their local critical temperature $T_{\nu c}^{i,j}$, where i, j are the neighbouring sites of the square lattice and $\nu = x, y$ is the direction identifying the resistor bond. Specifically, a Gaussian distribution of critical temperatures $T_{\nu c}^{i,j} \neq 0$ was assumed, characterized by a given average value μ and a variance σ. An extended analysis also showed that different statistical distributions provide more or less equivalent physical results [48] and therefore, for the sake of simplicity, we here only consider Gaussian distributions of local critical temperatures. A more precise description of transport data also led to distinguishing between the Gaussian distribution of bulkier (puddle-like) regions, with a mean value of the SC critical temperature (μ_b) slightly higher than the global T_c , and a Gaussian distribution of the filamentary regions where the average SC temperature (μ_f) is slightly lower and, in general, more broadly distributed.Once the random inhomogeneous structure of the system has been specified, we define R_m as the resistance of the metallic matrix, while for the superconducting bonds, which include both the filamentary and the puddle-like regions, we assign a resistance value such that $R_{\nu}^{i,j}(T > T_{\nu c}^{i,j}) = R_s$ and $R_{\nu}^{i,j}(T < T_{\nu c}^{i,j}) = 0$. The standard deviations, σ_f and σ_b, relative to the two Gaussian distributions for the filamentary and puddle-like SC regions, determine the extension in temperature of the resistance tail, while the spatial filamentary structure of the SC cluster is crucial to recover the $R(T)$ approaching T_c with a long slowly vanishing tail.

So far, the discussion of the consequences of filamentarity on transport has focused only on the metallic phase stressing the 'tailish' behaviour of $R(T)$ as the signature of filamentary SC. In this work, we more directly address the issue of the superconducting response of the system by generalizing the RRN to finite frequencies thereby calculating the complex conductivity of the system. Thus, we assign to each bond a complex impedance $Z_{\nu}^{i,j} = R_{\nu}^{i,j} + i\omega_0 L_{\nu}^{i,j}$, where ω_0 is the frequency of the circuit and $L_{\nu}^{i,j}$ is either the inductance of the superconducting bonds, L_s, or that of the metallic matrix, L_m. The extension to finite frequencies of the RRN model into a Random Impedance Network (RIN) model was already investigated in its effective medium analytical solution [36,37], where the information on the geometrical structure of the cluster was, however, completely neglected. Here, we calculate exactly the global effective impedance $Z_{\text{tot}} = R_{\text{tot}} + i\omega_0 L_{\text{tot}}$ of the lattice by solving the Kirchhoff and Ohm laws of the network (see Appendix A.1). That allows us to account for the role played by the SC cluster geometry that we generated using a diffusing limited aggregation algorithm, discussed in Appendix A.2. In order to be quantitative, in the present work we will take as a case study the resonant-microwave measurements performed on LAO/STO interfaces, which we discuss in the next Sections. That is why, in our numerical study, we will fix the frequency to the experimental resonant frequency $\omega_0/2\pi = 0.36\,\text{GHz}$. Here, we are interested in the linear response of the system, neglecting possible non-linear effects that might arise, e.g., from currents exceeding

critical currents in the system. We are thus implicitly assuming that $I_\nu^{i,j} < I_{\nu c}^{i,j}$ in each bond, $I_\nu^{i,j}$ being the current flowing in the (i,j)-th bond in the direction ν and $I_{\nu c}^{i,j}$ the local critical current. Our goal is to identify the physical ingredients needed to reproduce the specific peculiarities found in experiments and summarized in the next Section.

4 LaAlO$_3$/SrTiO$_3$ interfaces

In SrTiO$_3$-based heterostructures, the carrier density of the 2DEG formed at the interface can be tuned by a gate voltage V_G. Despite their very clean and regular structure, these heterostructures have revealed an intrinsic tendency to electronic phase separation [16], leading to the formation of an inhomogeneous superconducting state with a filamentary character [49,50]. This happens even for the [001] orientation, i.e., when the interface is orthogonal to the c-axis of both LAO and STO; henceforth, we will always refer to [001] LAO/STO samples. Tunnelling [32,51], atomic force microscopy [52], and critical current experiments [53] provide clear evidence of an inhomogeneous superconducting condensate at the LAO/STO interface. Direct measurements of the superfluid density via SQUID measurements [54] showed that $J_s(T)$ does not follow neither BCS nor BKT prescriptions; the behaviour was instead well captured once the inhomogeneous character of the condensate was considered [49]. Transport measurements report further signs of inhomogeneity, with a percolating metal-to-superconductor transition where a sizable fraction of the 2DEG remains metallic down to the lowest accessible temperature [21, 48–50]. The resulting filamentary state, where the SC regions live on 100-nanometer length scales [55], coexist with the linear SC regions identified on the micron scale at structural domain boundaries [56,57]. The length scales at play are in perfect agreement with the effective medium approach used in [49], which accounts for the intrinsic averaging operated by the SQUID device over the micrometric scale.

In a previous publication [58], we reported the results of resonant microwave transport experiments at the lowest temperatures. Dynamical transport measurements provide in fact direct access to the superfluid stiffness J_s. When $\hbar\omega_0 \ll \Delta$, the system behaves as a RLC resonant circuit, allowing to identify the inductive response with the superfluid stiffness through $J_s = \frac{\hbar^2}{4e^2 L_k}$, where L_k is the kinetic inductance of the circuit; hence $\sigma_2 \propto \frac{1}{\omega_0 L_k} \propto J_s$ accounts for the inertia of Cooper pairs while σ_1 accounts for the transport of unpaired electrons, in analogy with optical conductivity. From a comparison between the gap and the superfluid stiffness energy scales, we identified two distinct regimes: an overdoped (OD) regime (i.e., with a carrier density higher than the one corresponding to the maximum superconducting critical temperature T_c), in which the LAO/STO system has the character of a dirty but rather homogeneous two-dimensional (2D) superconductor and an underdoped (UD) regime (i.e., with a carrier density lower than the one corresponding to the maximum superconducting critical temperature T_c), where the superconducting state closely resembled a disordered 2D Josephson-junction array (see Fig. 4 of Ref. [58]).

In this work, we consider the resonant microwave transport experiments over a broad temperature and carrier density range. The correspondence between gate voltage and carrier density is given in Fig. 5 of Ref. [58]. By measuring both the complex conductivity, i.e., $\sigma = \sigma_1 - i\sigma_2$, and the DC resistivity, we study the superconductor-to-metal transition characterizing the emerging filamentary superconducting state, via the temperature dependence of its superfluid stiffness J_s and conductance σ_1.

In Fig. 1, we report the DC resistivity (green) and complex conductivity data (real part in black, imaginary part in red) for a LAO/STO sample. In particular, Fig. 1(a) and 1(b) show two paradigmatic examples for the OD (gate voltage $V_G = 50$ V) and UD ($V_G = 20$ V) regimes, respectively. The data of DC resistivity and complex conductivity in a wider range of back-gate
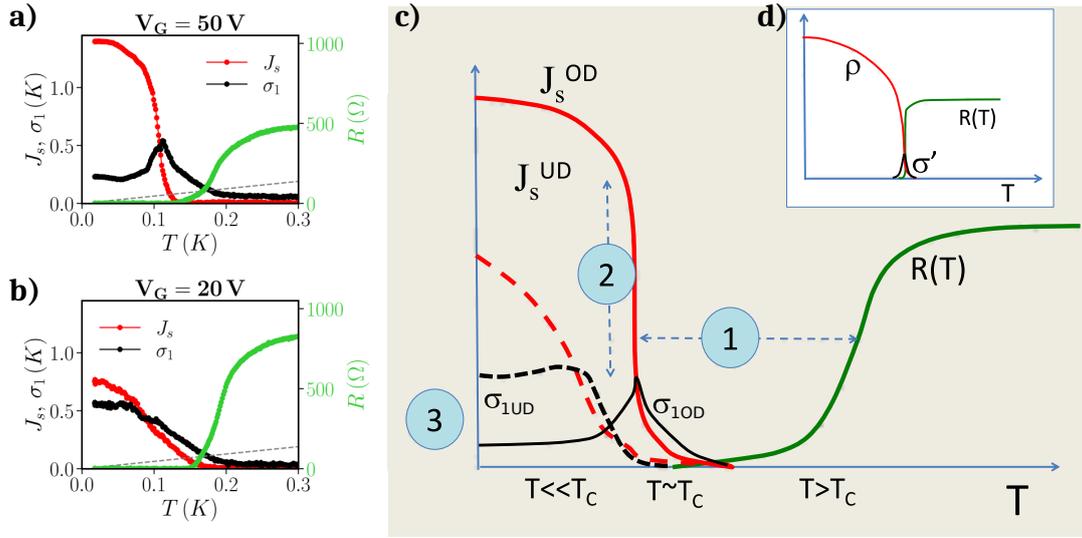
Figure 1: DC resistance (green), superfluid stiffness $J_s \propto \sigma_2$ (red) and optical conductance σ_1 (black) as functions of temperature. (a) Experimental data for a gate voltage $V_G = 50\,\text{V}$ (OD) and (b) for $V_G = 20\,\text{V}$ (UD). The grey dashed line is the BKT critical line $2T/\pi$. (c) Sketched summary of the observed features in the UD (dashed lines) and OD regimes (solid lines): (1) the broad and tailish transition of $R(T)$ coincide with a very gradual increase of J_s at $T \sim T_c$; this results in a wide separation between the two, paradigmatic of a percolating yet filamentary superconducting cluster; (2) increase of J_s at $T \lesssim T_c$, more abrupt in OD systems than in the UD ones, thus signalling the more or less homogeneous nature of the superconductor at different fillings; (3) the substantial residual value of σ_1, more important in the UD case yet more peaked in the OD. Those features are clearly at odds with the scenario of a dirty yet homogeneous 2D superconductor, schematically reported in (d).

voltage, from 8 V up to 50 V, are presented in Fig. 8 of Appendix B.

In Fig. 1(c), we schematically summarize the peculiar features found in the two doping regimes of LAO/STO samples. Besides the broad transition and tailish behaviour of the resistance curve $R(T)$ (green solid line), near the temperature T_c that marks the transition to a filamentary superconducting state [21, 48–50], we outline three main peculiar features:

(1) going through the metal-to-superconductor transition, an unusual and surprising separation appears between the temperature at which the resistivity vanishes and that relative to the onset of a sizable superfluid stiffness. Both $R(T)$ and $J_s(T)$ show a long tail, symptomatic of a percolating filamentary superconducting state, still too fragile to establish a 2D rigid condensate;

(2) lowering the temperature below T_c, the superfluid stiffness shows an increase, steep in the OD case and more gradual in the UD regime; notice that in the OD regime, the steep increase of J_s occurs at a temperature much lower than T_c;

(3) at $T \ll T_c$, the real part of the conductance $\sigma_1(\omega_0, T)$ takes a significant residual value. This last feature marks the persistence of a sizable fraction of normal metal down to the lowest temperatures, further supporting the idea of an inhomogeneous superconducting state.

This last feature marks the persistence of a sizable fraction of normal metal down to the lowest

temperatures, further supporting the idea of an inhomogeneous superconducting state.

Finally, in Fig. 1(d) we sketch the behaviour of the same quantities as a function of temperature within the BKT scenario in the presence of moderate disorder [59]. The BKT scheme clearly fails to reproduce the main features of the data. Even the seeming jump experimentally observed in the superfluid stiffness, e.g., at $V_G = 50$ V, cannot be interpreted as the paradigmatic hallmark of the BKT transition, rather expected at the intercept with the $2T/\pi$ critical line [dashed-grey line in Fig. 1(a)].

In what follows, we present our extensive resonant microwave transport analysis. We show the actual occurrence of these three peculiar features in the experimental data, and we discuss our theoretical analysis to extract information about the structural characteristics of the superconducting system throughout the temperature and carrier density range considered. It is worth noting that the three peculiar features summarized above are indeed characteristic of the rather disordered sample, whereas in more homogeneous ones the long tails in $R(T \sim T_c)$ and in $J_s(T \sim T_c)$, and the huge σ_1 residue at $T \ll T_c$ are less enhanced and one would recover an intermediate phenomenology between a standard BCS scenario [Fig. 1(d)] and the one presented here [Fig. 1(a)-(c)]. Nonetheless, although this sample may not be representative of every LAO/STO interface, it offered the motivation to study the effect of filamentarity and to generalize its consequences, without the burden of worrying about microscopic details. Indeed, measurements on different samples could lead to different resistive and superfluid responses having, in general, a different amount of *mesoscopic* disorder, which is intrinsic and unavoidable in LAO/STO heterostructures. Our theoretical framework provides insights both into the amount and the spatial distribution of this emerging mesoscopic inhomogeneity. For the present disordered sample, our theoretical investigation provides a coherent rationale for the observed peculiar experimental features in terms of a filamentary superconducting structure embedded in a metallic matrix and following their evolution with carrier density and temperature.

4.1 Resonant microwave transport experiment

In this work, we used the same sample and experimental setup of Ref. [58]. While in [58] only the data at the lowest temperature were presented, here we perform a complex conductivity analysis of the back-gated [001] LAO/STO sample throughout an extensive carrier density and temperature range. We refer the reader to Appendix B and [58] for further experimental details.

In Fig. 2b and c we report the real and imaginary part of the complex conductivity as a function of temperature for a resonant frequency $\omega_0/2\pi = 0.36$ GHz and several values of the gate potential. Panel (c) reports the imaginary part of the conductivity $\sigma_2(\omega_0, T)$, proportional to the superfluid stiffness, displaying two markedly different temperature trends, according to the applied gate voltage. In the OD regime, with gating between 28 V and 50 V, the superfluid stiffness grows slowly with reducing the temperature below 0.16 K and then rapidly increases with a downward curvature between 0.11−0.13 K. In the UD regime, from 26 V down to 8 V, the superfluid stiffness grows much more gradually, with an upward curvature down to lower temperatures 0.04−0.07 K. A similar dichotomous behaviour is observed in the real part of the conductivity $\sigma_1(\omega_0, T)$ (panel b): in the OD regime, a rather sharp peak is observed at temperatures corresponding to the rapid increase of the superfluid stiffness, while in the UD regime, $\sigma_1(\omega_0, T)$ presents a much broader peak or no peak at all. In both cases, however, the real part of conductivity stays finite at the lowest temperatures, assuming values that are non-monotonic and maximal around gate voltages $\sim 20 - 24$ V.

This crossover is even more evident if one looks at the whole picture as a function of the gate voltage. While the voltage dependence of the critical temperature T_c vs V_G (green dots in Fig.2a) does not give any clear indications, the temperature at which σ_1 reaches its maximum
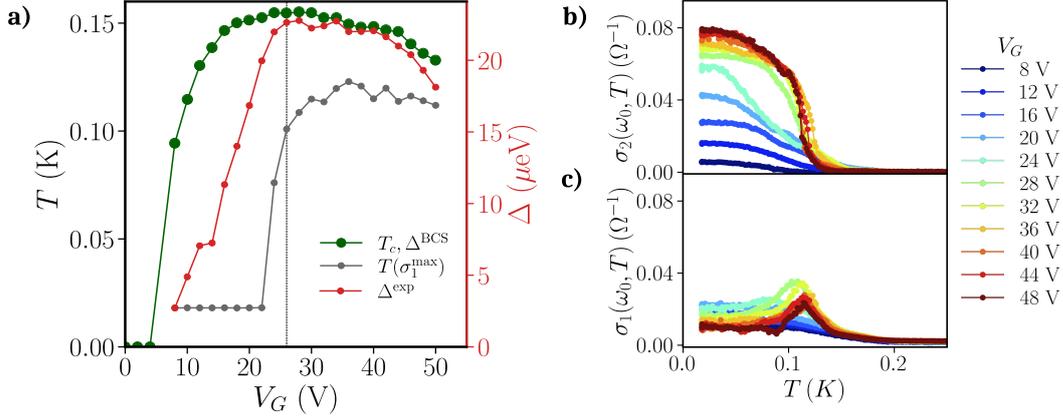
Figure 2: (a) Critical temperature dome T_c as function of the gate voltage V_G (green dots) experimentally measured in LAO/STO interfaces. In the same plot we compared $T_c(V_g)$ with the extrapolated temperature of the peak in σ_1 in Kelvin ($T(\sigma_1^{\mathrm{max}}$ grey dots). Finally, in red (right axis), we display $\Delta^{\mathrm{exp}} = 4e^2 J_s R_{\mathrm{N}}/\hbar\pi$. In a bare BCS scenario, this should be proportional to the T_c dome, i.e., $\Delta^{\mathrm{BCS}} = 1.76 k_B T_c$ (right axis). The dashed vertical line indicates the crossover from the UD and the OD system at $V_G = 26$ V. (b) The imaginary, $\sigma_2(\omega_0, T)$, and (c) the real part, $\sigma_1(\omega_0, T)$, of the complex conductivity measured as functions of temperature and at different gate voltages. The microwave frequency experimentally used, i.e. the circuit's resonant frequency, is $\omega_0/2\pi = 0.36$ GHz.

value ($T(\sigma_1^{max})$ in grey) gives a rather clear idea of the crossover between the UD to the OD regimes. At the same time, the saturating value of $J_s^{\mathrm{max}} = J_s(T \to 0)$ shows how the system falls outside the theoretical framework of conventional BCS superconductors. Within the standard BCS scenario, the superconducting gap at zero temperature Δ_0 is expected to follow the T_c dome, being $\Delta_0 \approx 1.76 k_B T_c$; in Fig. 2a, we report in green Δ^{BCS} (right axis). On the other hand, assuming the dirty limit, the same gap should behave as $\Delta_0 \sim J_s(0) R_N$. We display in red (right axis) the quantity $\Delta^{\mathrm{exp}} = 4e^2 J_s R_{\mathrm{N}}/\hbar\pi$, to underline once again the discrepancy of such measurements with the BCS scenario [58]. The deviation observed, i.e., $\Delta^{\mathrm{exp}} < \Delta^{\mathrm{BCS}}$, is consistent with our idea of filamentary superconductivity presented in Section 2.

5   Theoretical results and their interpretation

Despite its conceptual simplicity, the RIN model is complete and flexible enough to reproduce the rather unconventional trends experimentally observed. By lowering T, the bonds with $T_c^{i,j} \geq T$ become superconducting, so that the SC network nucleates inside the normal-metal matrix with specific signatures depending on the geometric structure (more or less dense filaments), the disorder (represented by the width of the random distribution of $T_c^{i,j}$), and on the characteristics of the mesoscopic metallic/superconducting regions, as modelled by the parameters R_m, L_m, R_s, L_s. We anticipate that the choice of the values for the "microscopic" resistors and impedances are made to match the experimental measurements at our disposal assuming an angular frequency $\omega_0 = 2 \times 10^9 \, \mathrm{s}^{-1}$. More details can be found in Appendix C. Our goal is to infer and understand *micro- and mesoscopic* features of the electronic condensate from the *macroscopic* phenomenology given by transport measurements.

5.1 Effect of the geometry and disorder on the resistance and superfluid behaviours

The geometry of the superconducting cluster and the widths σ_b and σ_f of the random distribution, $P(T_c^{i,j})$, of the individual SC bonds critical temperatures $T_c^{i,j}$ encode the most prominent peculiar property (1) of the LAO/STO superconductor [Fig. 1(c)]. Starting from the normal state, by lowering the temperature, the resistance smoothly decreases, mostly due to the puddle-like regions becoming superconducting; if these were absent, with a SC cluster only made of filaments, the decrease of $R(T)$ would indeed start in a much sharper way. We thus investigated the relevance of both filaments and puddles.

The filamentary structure is built via a diffusion-limited aggregation (DLA) algorithm [13, 48] (see Methods for details). We stress here that extensive iterations of the DLA algorithm would produce a fractal-like geometrical structure, but in our case this is instead a mere technical tool to produce a random assembly of filamentary structures on our finite square-lattice cluster. The superconducting puddles, with a given radius r_{pd}, are afterwards added to the cluster, to reach the total superconducting density w we fixed. It follows that the larger r_{pd}, the less numerous the puddles will be. Their role is fundamental in explaining the first downturn of $R(T)$ but, once they became superconducting, their size is almost irrelevant to the complex conductivity properties. Indeed, the superfluid rigidity and the residual dissipation are mainly determined by the structure and the density of the filamentary components of the superconducting cluster, while the puddles play a minor role. Specifically, by lowering T, the filamentary structures become more and more superconducting and, when a superconducting percolating path forms, the resistance vanishes at the global critical temperature T_c, $R(T_c) = 0$. Due to the nearly one-dimensional (1D) character of the filamentary structures and their poor connectivity, the resistance stays low but finite until the very last resistor of the percolating path is switched off. That explains why the filamentary geometry is crucial to account for the tailish behaviour of $R(T)$.

How broad the transition and how long the tail depends instead on the width $\sigma_{f,b}$ of the Gaussian distribution of the $T_c^{i,j}$s, accounting for the microscopic impurities generically present in real systems. At the same time, the filamentary percolating cluster is formed by a low fraction of superconducting bonds with a nearly 1D structure. Therefore, they cannot result in a large rigidity of the superconducting condensate. Indeed, a rather small $\sigma_2 \propto J_s$ is found for $T \lesssim T_c$. The long tails observed in LAO/STO interfaces in both $R(T)$ and $J_s(T)$, which also lead to the apparent separation of the two curves, find in this way a natural explanation [Fig. 1(c)].

By further lowering the temperature, more and more bonds in the random filamentary subset become superconducting, leading to the more or less rapid growth of the condensate rigidity depending on the specific features of the superconducting subset. Quite obviously, the more or less dense (and interconnected) character of the filamentary structure determines the more or less rapid growth and the intensity of the condensate rigidity J_s (See Appendix A).

5.2 Effects of the internal character of the mesoscopic metallic and superconducting regions

Besides the effect of the geometry and density of the filaments, the more or less rapid growth of $\sigma_2 \propto J_s$ at some $T < T_c$ – peculiarity (2) of Fig. 1(c) – is also dependent on the internal rigidity of the individual mesoscopic superconducting bonds, via their parameter L_s. The smaller the local inductance L_s, the more rigid the individual mesoscopic superconducting bond and the more rapidly and intensely the overall rigidity grows.

In Fig. 3, we show how both the two experimentally observed regimes, OD and UD, can be successfully captured by fixing the geometric structure of the superconducting cluster, shown
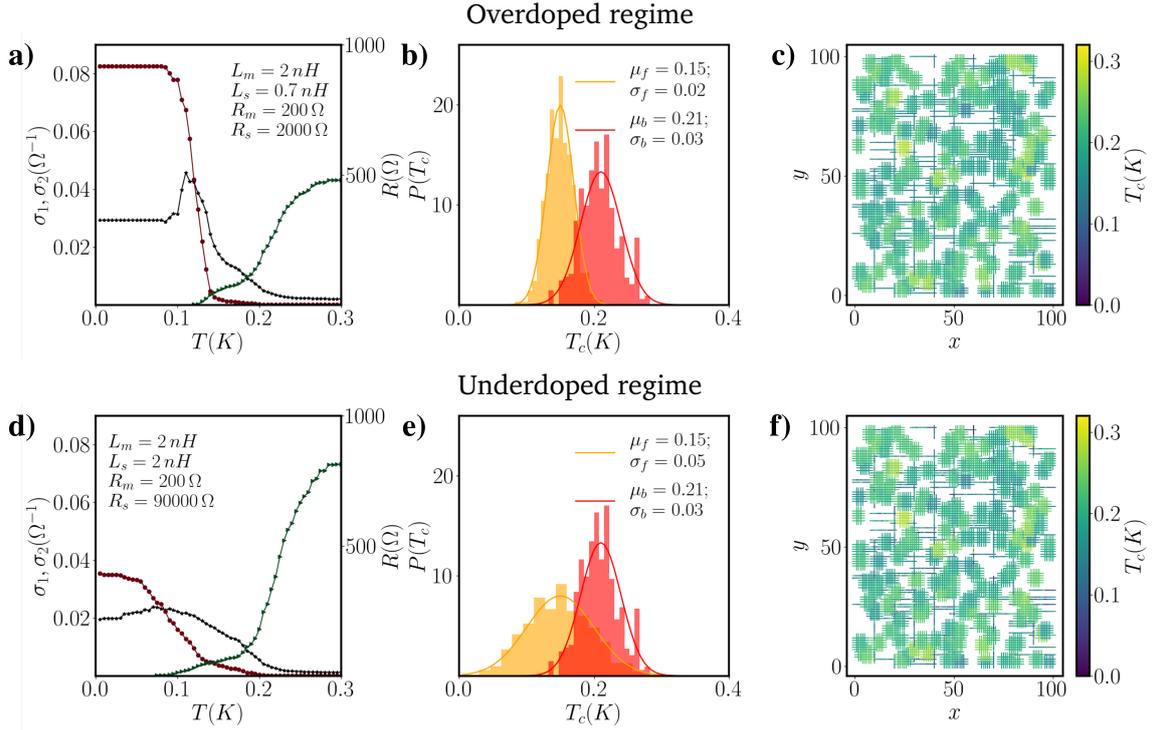
Figure 3: Temperature dependence of complex conductivity and DC resistivity calculated with the RIN model to describe the (a) OD and (d) UD system (real part in black, imaginary part in red and DC resistivity in green). The superconducting structure to which they correspond are shown in panels (c) and (f) respectively; the colour code refers to the local critical temperatures, yellow to blue regions are superconducting, while the metallic matrix is in the white background. Both cases in (a) and (d) refer to the same geometry of the underlying RIN, with total SC density $w = 0.43$, and the same parameters of the metallic matrix $R_m = 200\,\Omega$, $L_m = 2\,\text{nH}$. Instead, the parameters of the superconducting cluster are different: (a) OD: $R_s = 2000\,\Omega$ $L_s = 0.7\,\text{nH}$ (d) UD: $R_s = 90000\,\Omega$ $L_s = 2\,\text{nH}$ as well as the width of the $T_c^{i,j}$ distribution for the filamentary SC regions, as visible from the corresponding panels in which (b) OD: $\sigma_b = 0.03\,\text{K}$, and $\sigma_f = 0.02\,\text{K}$ and (e) UD: $\sigma_b = 0.03\,\text{K}$, and $\sigma_f = 0.05\,\text{K}$. This last difference is highlighted in panels (c) and (f) where we show the corresponding distributions of $T_c^{i,j}$ for the puddles and the filamentary structure.

in Figs. 3(b) and 3(e), whose filamentary character keep $R(T)$ and $J_s(T)$ well separated. By simply varying the value of the inductances L_s and the width of the random distribution $P(T_c^{i,j})$ for both the filamentary, σ_f, and the puddle-like SC regions, σ_b. For the OD regime [see Fig. 3(a)], by fixing $L_s = 0.7\,\text{nH}$, $\sigma_f = 0.02\,\text{K}$, and $\sigma_b = 0.03\,\text{K}$, we recover both the steep increase of $\sigma_2(T)$ (red curve) and the peak of the optical conductivity $\sigma_1(T)$ (black curve) found experimentally. At the same time, for the UD regime [see Fig. 3(d)], we recover the slow increase of $\sigma_2(T)$ as well as the much broader peak of $\sigma_1(T)$ by employing a larger value of $L_s = 2.0\,\text{nH}$ and ima slightly wider distribution of critical temperatures for the filamentary SC bonds, with $\sigma_f = 0.05\,\text{K}$ [see Figs. 3(f) and 3(c)]. By comparing our calculations with the experimental results, we can affirm that: a) disorder, i.e., the width of the $T_c^{i,j}$ distributions, is comparatively larger in UD systems and b) the local mesoscopic superconducting regions, in the UD regime, have a smaller intrinsic rigidity, i.e., a larger inductance, likely as a consequence of a lower carrier density.

Finally, we address the issue of the substantial residual normal-state real conductivity at

$T \ll T_c$ [peculiarity (3) of Fig. 1(c)]. According to our analysis (see also Appendix A and C), we found that at low temperatures the resistance of the residual metallic bonds largely determines the real (dissipative) part of the complex conductivity, with the residual σ_1 being inversely proportional to R_m. At the same time, a sparser geometry of the filaments will result in a more abundant residual metallic component, hence enhancing the dissipation in the superconducting state. The use of different values for the internal character of the resistors, R_s and R_m, reflects the presence in [001] LAO/STO samples of two different types of carriers, with different mobilities, whose relative density depends on the gating applied (see Appendix C for details).

6   Discussion and concluding remarks

In summary, we presented here a detailed theoretical interpretation of the complex conductivity experimentally measured in a [001] LAO/STO interface. Our theoretical analysis shed light on the intriguing peculiar features experimentally observed, revealing that they stem from the interplay between the filamentary structure of the superconducting cluster, embedded in a normal metal, and disorder, resulting in a random distribution of local critical temperatures. The main consequence is that the superfluid properties, in particular, the rigidity of the condensate, primarily depend on the geometrical structure of the superconducting cluster and only secondarily on the density of the superfluid matter. This result is highly nontrivial since the concepts of superfluid density and stiffness are often used as synonymous. We point out that, by neglecting the role of phase fluctuations, that reduces the superfluid stiffness without affecting the density of carriers, this identity is only true for homogeneous systems and can be strongly violated when the system is highly inhomogeneous. Our LAO/STO interface can therefore be taken as an example for a new paradigm of superconducting matter. We are aware that other interfaces and low-dimensional superconductors do not always display the same peculiar features, but we here point out precisely the physical ingredients leading to such anomalous behaviours, which may or may not be present depending on the amount of inhomogeneous charge distribution (resulting in regions with different local critical temperatures) and its more or less filamentary spatial structure.

The very starting point of the model, where disorder is encoded both in the randomly generated filamentary-puddle superconducting cluster and in a random distribution of local critical temperatures, may seem at odds with the very clean and structurally ordered LAO/STO interface. However, the presence of filamentary superconducting regions in [001] LAO/STO interfaces has been experimentally assessed both at the micron [56,57] and at the submicron [55] scales and it is supported by many experimental and theoretical evidence.

The main message of this work is that the peculiar features of the complex conductivity data arise from the inhomogeneous filamentary character of the superconducting regions and the main differences between OD and UD systems stem both from the more or less broad distribution of local T_c's (i.e from the relative relevance of disorder) and from the microscopic characteristics resulting in different values of the parameters L_s, L_m, R_s, R_m. In particular, we were able to identify the specific physical effects of each handle of the model on macroscopic transport: the resistivity and inductance of the various regions, how rapidly the normal metal becomes superconducting by decreasing T, due to the width of the $T_c^{i,j}$ distribution associated with the microscopic disorder, and so on.

Finally, beyond its theoretical understanding, the study of inhomogeneous filamentary electronic condensates can pave the way for a systematic control and exploitation of superfluid systems with extremely small phase rigidity. This may result in interesting applications for sensors; systems with stiffness that can be tuned by gating and/or temperature; or where

the features of a Josephson-junction array can continuously be tuned from nearly homogeneous BCS to quasi-1D superconductors. Last but not least, filamentary superconductors in the presence of large Rashba spin-orbit coupling could provide a new path for the emergence and observation of Majorana fermions [60].

Acknowledgements

Author contributions   G.S. and A.J. performed the measurements assisted by N.B. Samples were fabricated by P.K. and E.L. under the supervision of A.D., R.C.B., A.B., and M.B., G.S., A.J., and N.B. carried out the analysis of the results. S.C. and M.G. elaborated on the model and the generalization of the RRN to finite frequencies. G.V. and I.M. performed the theoretical calculations. The manuscript was written by S.C., M.G., G.V., I.M., and N.B. with contributions and suggestions from all coauthors.

Funding information   S.C. and M.G. acknowledge financial support from the Italian Ministero dell'Università e della Ricerca, through the Project No. PRIN 2017Z8TS5B, the PNRR project 'Topological Phases of Matter, Superconductivity, and Heterostructures' Partenariato Esteso 4 - Spoke 5 (n. PE4221852A63A88D), and from the 'University Research Projects' of the Sapienza University of Rome: 'Superconductivity, inhomogeneity and novel phenomena in two-dimensional materials' (n. RM11916B56802AFE), 'Equilibrium and out-of-equilibrium properties of low-dimensional disordered and inhomogeneous superconductors' (n. RM12017 2A8CC7CC7), 'Competing phases and non-equilibrium phenomena in low-dimensional systems with microscopic disorder and nanoscale inhomogeneities' (n. RM12117A4A7FD11B), 'Models and theories from anomalous diffusion to strange-metal behavior' (n. RM12218162CF 9D05). I.M. acknowledges the Carl Trygger foundation through grant number CTS 20:75. N.B. acknowledges the ANR QUANTOP Project-ANR-19-CE470006 grant.

A   RIN equations and geometry of the superconducting network

A.1   RIN equations and algorithm

We present here the equations for the bonds and nodes of the RIN model. A sketch of the system is shown in Fig. 4. We use open boundary conditions to have a more realistic description of a finite sheet of impedances with an external applied voltage V^{ext} at the left-right extrema. It is worth noting that the parent model of the RIN, namely the RRN model, is recovered for $\omega = 0$ so $Z_\nu^{i,j} = R_\nu^{i,j}$.

Kirchoff's and Ohm's equations are solved linearizing the problem as

$$\hat{A} \cdot \vec{X} = \hat{B} \tag{1}$$

where $\hat{B}$ contains the known terms, i.e., the external voltage, which can be either V or zero, $\hat{A}$ is a sparse matrix, whose elements of a single row can contain at most three non-zero terms, which can be either ± 1 or $Z_{i,j}$; $\vec{X}$ is the vector containing all the unknown (complex) currents $I_\nu^{i,j}$, with $\nu = x, y$, and (complex) potentials $V_{i,j}$. Note that the boundary condition V^{ext} is a real value and the total number of complex equations is $N^2 + 2N(N-1) = 3N^2 - 2N$, where N is the linear size of the network. Once Eq. 1 is solved for $\vec{X}$, we compute the effective impedance of the whole system simply as:

$$Z_{\text{tot}} = \frac{V^{\text{ext}}}{\sum_{i,j} I_x^{i,j}} (N-1) \tag{2}$$

Figure 4: Scheme of the impedance network with open boundary conditions. The currents are positive when entering in the node, negative if exiting (upper left sketch). Each impedance in the ν direction is $Z_\nu = R_\nu^{i,j} + i\omega L_\nu^{i,j}$. The various colors correspond to the 5 different domains: the bulk domain 1 is in black, the upper and lower edges corresponds respectively to domains 2 and 3 in green ($i = 1$) and blue ($i = N$) and a potential difference V is applied to the left and right edge, the former corresponding to domain 4 in red ($j = 1$), the latter in orange is domain 5 ($j = N$).

The equations for the 5 different domains and showed with different colors in in Fig. 4 are the following.

Domain 1 - bulk (black):

$$\begin{cases} V_{i,j} - V_{i,j+1} - Z_x^{i,j} I_x^{i,j} = 0 \\ V_{i,j} - V_{i+1,j} - Z_y^{i,j} I_y^{i,j} = 0 \\ I_x^{i,j-1} - I_x^{i,j} + I_y^{i-1,j} - I_y^{i,j} = 0 \end{cases} \tag{3}$$

where i, j runs over $2, N - 1$.

Domain 2 - upper edge ($i = 1$) (green):

$$\begin{cases} V_{1,j} - V_{1,j+1} - Z_x^{1,j} I_x^{1,j} = 0 \\ V_{1,j} - V_{1+1,j} - Z_y^{1,j} I_y^{1,j} = 0 \\ I_x^{1,j-1} - I_x^{1,j} - I_y^{1,j} = 0 \end{cases} \tag{4}$$

where $i = 1$ and j runs over $2, N - 1$

Domain 3 - lower edge ($i = N$) (blue):

$$\begin{cases} V_{N,j} - V_{N,j+1} - Z_x^{N,j} I_x^{N,j} = 0 \\ I_x^{N,j-1} - I_x^{N,j} + I_y^{N,j-1} = 0 \end{cases} \tag{5}$$

$i = N$ and j running over $2, N - 1$.

Domain 4 - left edge ($j = 1$) (red): Boundary conditions: the nodes are all set to a V^{ext} external potential, so the currents along y are all zero.

$$\begin{cases} V_{i,1} = V & i = 1, N \\ V_{i,1} - V_{i,2} - Z_x^{i,1} I_x^{i,1} = 0 & i = 1, N \\ I_y^{i,1} = 0 & i = 1, N - 1 \end{cases} \tag{6}$$

Domain 5 - right edge ($j = N$) (orange): Boundary conditions.

$$\begin{cases} V_{i,N} = 0 & i = 1, N \\ I_y^{i,1} = 0 & i = 1, N-1 \end{cases} \tag{7}$$

Note that the complex nature of such equations (if $\omega \neq 0$) doubles the actual number of unknown elements in Eq. 1. Hence, numerically, we double the matrix $\hat{A}$ in order to solve separately Eq. 1 for the real and imaginary parts. We use a sparse matrix to save only non-zero elements and we solve the two systems of linear equations using a standard algorithm for sparse linear systems [61].

A.2   Generation of the fractal

The generation of the superconducting filamentary structure is obtained by means of diffusion-limited aggregation (DLA) algorithm [13, 48]. Of course, this choice is arbitrary and it does not rest on a straight physical reason nor it aims at demonstrating that the superconducting regions have some defined fractal-like structure. It is simply a technical way to represent strongly inhomogeneous systems with space correlation and connectivity over large distances. The fractal-like structure is grown by diffusing from left to right n_{RW} random walk particles in a square of size $L_\square$ larger than the size ($L \times L$) of the square lattice network ($L_\square > L$), that we investigate in the complex conductivity calculations. We allow each of the n_{RW} to move r_{DLA} bonds (steps) to the right and y_{DLA} bonds up or down, with equal probability, whereas in the RRN calculations presented in Refs. [13, 48] $r_{DLA} = y_{DLA} = 1$. Hence, we can construct a more or less dense network of filaments just by tuning those parameters, keeping a higher fraction of the metallic residue without preventing percolation.
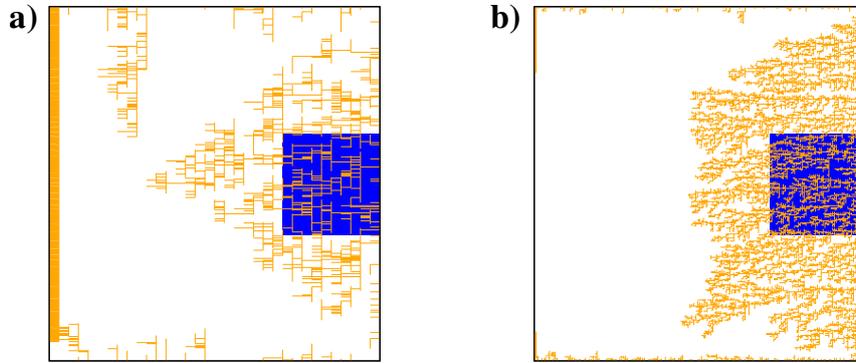
Figure 5: Examples of filamentary structures constructed via the "improved" DLA algorithm launching $n_{rw} = 15\,000$ diffusing particles across a 350×350 square lattice. In orange are shown the obtained clusters with (a)$r_{DLA} = 10$, $y_{DLA} = 10$ and (b) $r_{DLA} = 2$, $y_{DLA} = 2$. Highlighted in blue is the metallic region that defines the final 100×100 square lattice.

This procedure is iterated until the particle stops, as soon as it reaches the top, bottom or right edge where it sticks; if it reaches a site already occupied by one of the previously diffused particles, it takes a step back and stops thereby increasing the cluster of aggregated particles: the cluster obtained is defined by all the bonds connecting two stuck particles. From this super-network, a sub-network of size 100×100 is selected and it will be the superconducting backbone of the RIN. Then, patches of radius r_{pd} will be superimposed until a fraction w of superconducting resistors is reached. In Fig. 5, are shown two 250×250 different super-network constructed launching $n_{RW} = 15000$ particles. In panel a, the (orange) superconducting fractal is built from random walkers allowed to do $r_{DLA} = 10$ steps on the right and $y_{DLA} = 10$ steps

on the left, the same used for the results shown in Fig.3, while in panel b the constraints were $r_{DLA} = 2$, $y_{DLA} = 2$. In both panels, the region coloured in blue is the metallic background of the final 100×100 network.

For the sake of completeness, we show here how a denser fractal geometry modifies the superfluid and resistive responses. In Fig. 6 we present the RIN results obtained for a cluster constructed from a $r_{DLA} = 2$, $y_{DLA} = 2$ fractal, all other parameters being equal to the ones used in Fig. 3. By looking at panels a and d of Fig. 6 one can observe how the shapes of the curves σ_1, σ_2 as functions of the temperature are qualitatively different from their counterparts presented in Fig. 3. In particular, the saturating value of σ_2 is increased by the denser geometry of the underlying fractal. Concerning instead the optical conductivity σ_1, one can observe that the saturating value at $T = 0$ is unchanged with respect to the geometry of the fractal, whereas its generic behaviour and, particularly, its peak are non-trivially dependent on the filamentary geometry. That occurs despite the fact that the total number of superconducting bonds is the same in all four cases presented in Figs. 3 and 6, being $w = 0.43$, revealing once again the fallacy, in inhomogeneous systems, of the assumption that superfluid density is equivalent to superfluid stiffness. One can also note that the probability distributions $P(T_c)$ (panels b and e) are only slightly changed by the different geometry.

B Resonant microwave transport experiment

In this work, we used 8 uc-thick LAO layers grown on 3×3 mm^2 (001) STO single crystals by Pulsed Laser Deposition (PLD). The substrates were first treated with buffered HF to ensure a TiO_2 termination of the surface. The LAO layer was deposited at a temperature of 800 °C in an oxygen partial pressure of 1×10^{-4}mbar. PLD was performed with a KrF excimer laser at a rate of 1 Hz with an energy density of 0.56-0.65 J cm^{-2}. After the growth, a weakly conducting metallic back-gate of resistance $\sim$100 kΩ, to avoid microwave shortcut of the two-dimensional electron gas (2DEG) is deposited on the backside of the 200 μm thick STO substrate.

Resonant microwave transport measurements were performed using a setup identical to that described in Reference [58] and the same approach was used to extract the complex conductivity of the oxide 2DEG. In short, the LAO/STO sample was inserted into a parallel RLC electrical resonant circuit to perform microwave measurement in a reflection configuration as already used to probe the $SrTiO_3$ and $KTaO_3$ based superconducting interfaces [58, 62, 63]. Fig. 7 provides the equivalent sample electrical circuit. Inductor L_1 and resistor R_1 are Surface Mounted microwave Devices (SMD) and capacitor C_{STO} represents the contribution of the STO substrate itself in parallel with the 2DEG. Because of the high dielectric constant of STO at low temperature (i. e. $\epsilon \simeq 24000$), C_{STO} dominates the circuit capacitance. C_p are protective capacitors that avoid dc current to flow through L_1 and R_1 without affecting the resonance. A bias tee allows measuring both the dc and ac microwave transport properties of the 2DEG at the same time.

In the normal state, the sample circuit resonates at the frequency $\omega_0 = \frac{1}{\sqrt{L_1 C_{sto}}}$, which can be determined by measuring the reflection coefficient of the sample circuit $\Gamma(\omega) = \frac{A^{in}}{A^{out}}$. The resonance manifests itself as an absorption dip in the magnitude of $\Gamma(\omega)$ accompanied by a 2π phase shift. In the superconducting state, the 2DEG conductance acquires an imaginary part $\sigma_2(\omega) = \frac{1}{L_k \omega}$ that generates a shift of ω_0 towards high frequencies since the total inductance of the circuit becomes $L_{tot}(T) = \frac{L_1 L_k(T)}{L_1 + L_k(T)}$ (L_k is the kinetic inductance of the 2DEG). σ_2, or equivalently the superfluid stiffness $J_s(T)$ can thus be extracted from the resonance shift for all gate voltage values. Likewise, the depth of the resonance is controlled by the dissipation of the sample circuit and gives access to the temperature-dependent σ_1 of the 2DEG. In our experi-
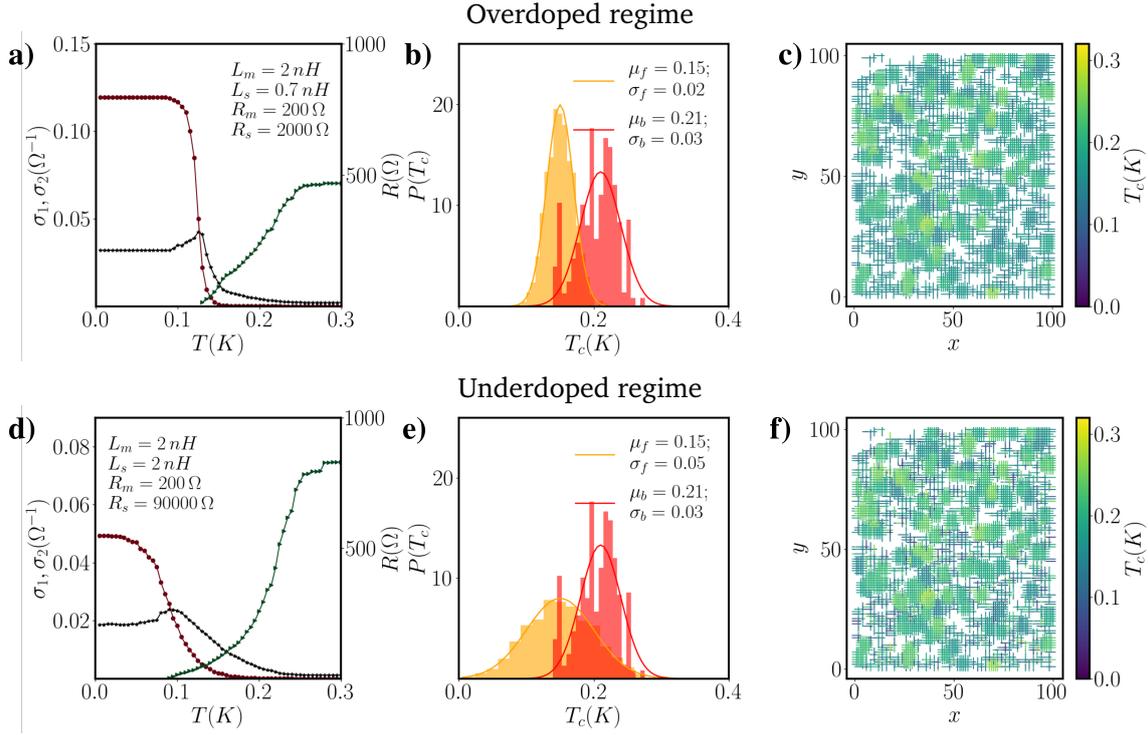
Figure 6: Temperature dependence of complex conductivity and DC resistivity calculated with the RIN model using the same parameters and probability distributions of Fig. 3 but with a denser fractal geometry. (a) Same parameters used to describe the OD regime and (d) the UD regime (real part in black, imaginary part in red and DC resistivity in green). The superconducting structure to which they correspond are shown in panels (c) and (f) respectively; the colour code refers to the local critical temperatures, yellow to blue regions are superconducting, while the metallic matrix is in the white background. Both cases in (a) and (d) refer to the same geometry of the underlying RIN, with total SC density $w = 0.43$, and the same parameters of the metallic matrix $R_m = 200\,\Omega$, $L_m = 2\,\text{nH}$. Instead, the parameters of the superconducting cluster are different: (a) OD: $R_s = 2000\,\Omega$ $L_s = 0.7\,\text{nH}$ (d) UD: $R_s = 90000\,\Omega$ $L_s = 2\,\text{nH}$ as well as the width of the $T_c^{i,j}$ distribution for the filamentary SC regions, as visible from the corresponding panels in which (b) OD: $\sigma_b = 0.03\,\text{K}$, and $\sigma_f = 0.02\,\text{K}$ and (e) UD: $\sigma_b = 0.03\,\text{K}$, and $\sigma_f = 0.05\,\text{K}$. This last difference is highlighted in panels (c) and (f) where we show the corresponding distributions of $T_c^{i,j}$ for the puddles and the filamentary structure.

Figure 7: Sketch of the microwave measurement setup.

ment, $J_s(T)$ and σ_1 can be directly extracted from the measured data for most of the regions of the phase diagram. Nevertheless, a calibration procedure can be applied to improve the precision of the measured quantities. It involves the realization of three known impedances of the sample circuit using three different gate voltage values. Details on the calibration method including a comparison between calibrated and uncalibrated data can be found in reference [58]. Uncertainty in the determination of the absolute value of σ_2 is estimated to be lower than 15% and the uncertainty on the absolute value of σ_1 is estimated to be lower than 10%. In both cases, the relative uncertainty in the temperature dependence is marginal.

For the sake of completeness, the temperature dependence of R, σ_1 and σ_2 for different back gate voltages ranging from 8 to 50 V are reported in Fig. 8.

C Choice of the parameters

Besides its overall geometrical structure – filamentary density and broadness of the $T_c^{i,j}$ distribution – the model is endowed with local parameters characterizing the transport properties of the individual mesoscopic regions, both the metallic (R_m, L_m) and the superconducting (R_s, L_s) ones. While L_m plays a minor role at any temperature, the resistivity of the metallic regions is crucial to determine the dissipative residual character of the system at low temperature: the lower is R_m, the higher is σ_1 [peculiarity (3) in Fig. 1(d)]. At the same time, the value of R_s is immaterial in the same low-T regime, but is fundamental in fitting the resistivity in the overall normal state $R(T > T_c)$. L_s, instead, determines the local rigidity of the condensate inside each mesoscopic superconducting region and plays a relevant role in determining the global rigidity: the lower is L_s the higher is the saturating value of σ_2 and the steeper is its growth. The choice of R_s and R_m becomes rather stringent in UD systems, where the large low-T dissipation requires rather small values of R_m, while $R(T)$ is rather large at high T. This requires the use of high values of R_s. Although this might seem at odds with the idea that the superconducting regions correspond to those regions where the electron density is higher, this choice of parameters can find a rationale by carefully considering the two families of carriers appearing in these LAO/STO interfaces. As discussed in Ref. [64], the 2DEG can be effectively described in terms of low-mobility and high-mobility carriers (LMC and HMC, respectively), the latter being ultimately responsible for the superconductivity onset. Indeed, one could argue that the density of states (DOS) of the superconducting regions, i.e., the effective electron mass, is large in spite of a small fraction of HMC and leads to a large local resistivity.

The mobility of these few carriers can be high if the small scattering compensates for the larger mass. At the same time, the metallic regions could have a small DOS, preventing them from becoming superconducting, but a large number of LMC can result in a comparatively smaller resistivity. To be more quantitative, the values extrapolated in [64] for the density of the two carriers n_1, n_2, for LMC and HMC, respectively, and their mobility μ_1, μ_2, give us the order of magnitude for the ratio R_m/R_s in the UD and OD regime. In particular, $\frac{R_m}{R_s} = \frac{n_1 \mu_1}{n_2 \mu_2} \sim 30$ for $V_G \simeq 50\,V$ and $\frac{R_m}{R_s} = \frac{n_1 \mu_1}{n_2 \mu_2} \sim 100$ for $V_G \leq 25\,V$ Finally, having an estimate of the effective masses of the two carriers, we can also extrapolate the order of magnitude of the ratio $L_2/L_1 = L_f/L_0$. Being $m_2^*/m_1^* \sim 0.07$ [65] and $n_1/n_2 \sim 100$, we have $\frac{L_2}{L_1} = \frac{L_f}{L_0} \simeq \frac{m_2^* n_1}{m_1^* n_2} \simeq 7$.

We report in Fig. 9 the real σ_1 and imaginary σ_2 parts of the conductivity and the DC resistivity R at various R_m and L_s for both underdoped and overdoped regimes. We use as a reference the cases discussed in Section 5, reporting panels a and d in Fig. 3 in panels a and d of Fig. 9, hence referring to Fig. 3c-d and d-e for the corresponding probability distributions $P(T_c)$ and the fractal geometry. As one can see looking at panels b and e of Fig 9, an increase of R_m acts differently on both σ_1, σ_2 curves. Whereas σ_2 is only suppressed by less than $0.01\,\Omega^{-1}$
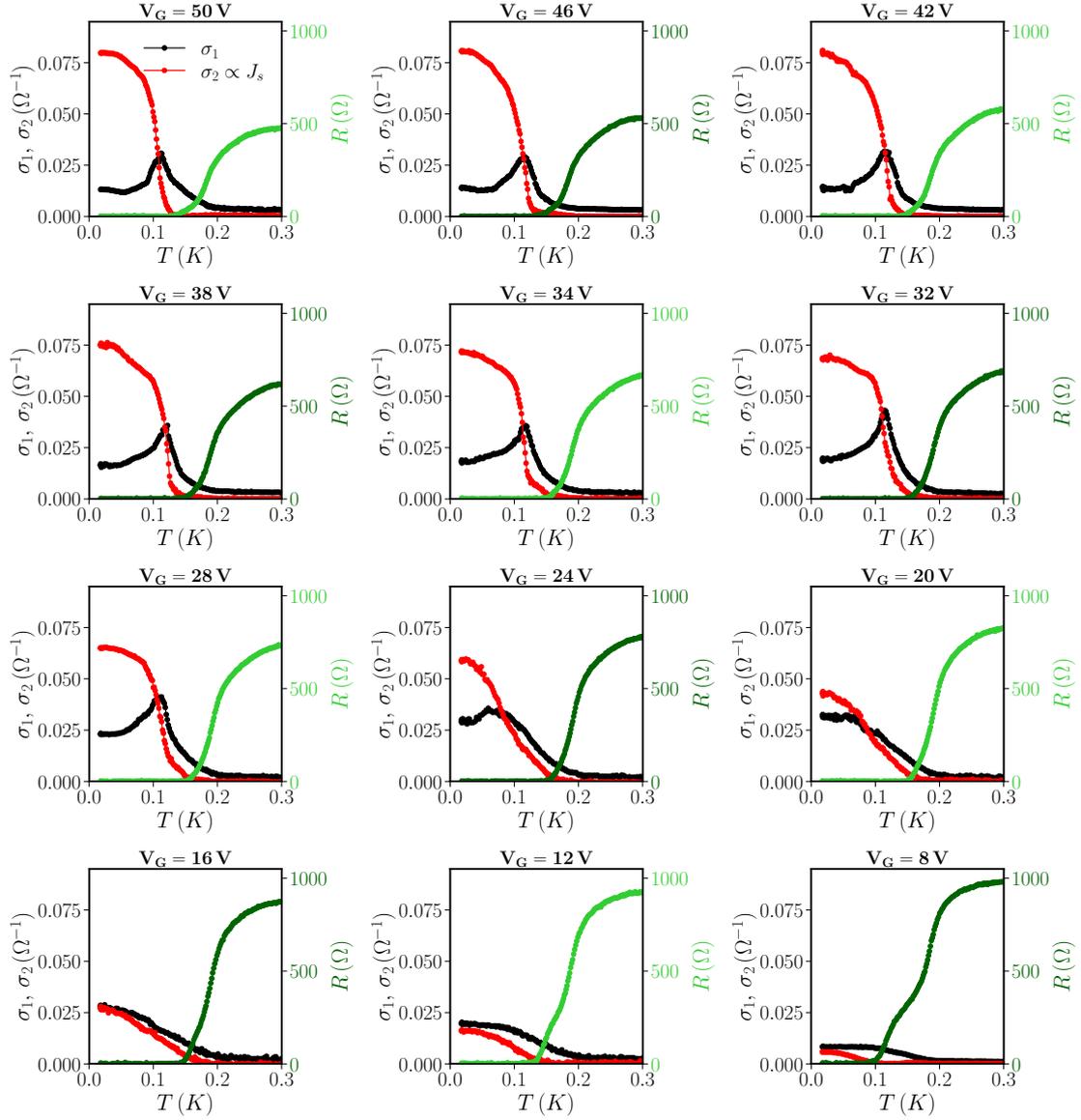
Figure 8: Experimental DC resistivity (green, right axis), real (black, left axis) and imaginary part of the conductance (red, left axis) plotted as a function of temperature for different values of the gate potential $8\,\mathrm{V} \leq V_G \leq 50\,\mathrm{V}$.

at $T = 0$, the real part of the conductivity, σ_1, gets significantly reduced by larger values of R_m. Conversely, a decrease in L_s from a value 2 nH to 0.7 nH results in the increase of both σ_1 and σ_2, acting primarily on the latter one. For the OD case, this effect can be observed by comparing panels c and a, whereas for the UD case, one can compare panels d and f of Fig. 9.

It is worth noting that even if R_m and L_s act on the behaviours in temperature of σ_1 and σ_2, they are not enough to capture the anomalous superfluid response experimentally observed. Together with the fractal geometry, indeed, also a slight difference in the probability distributions $P(T_c)$ – namely $\sigma_f = 0.02$ K for the OD case, $\sigma_f = 0.05$ K for the UD – of the filamentary component is required in order to capture the qualitative experimental behaviour of both the OD and UD regime, as already stated in Section 5.1.
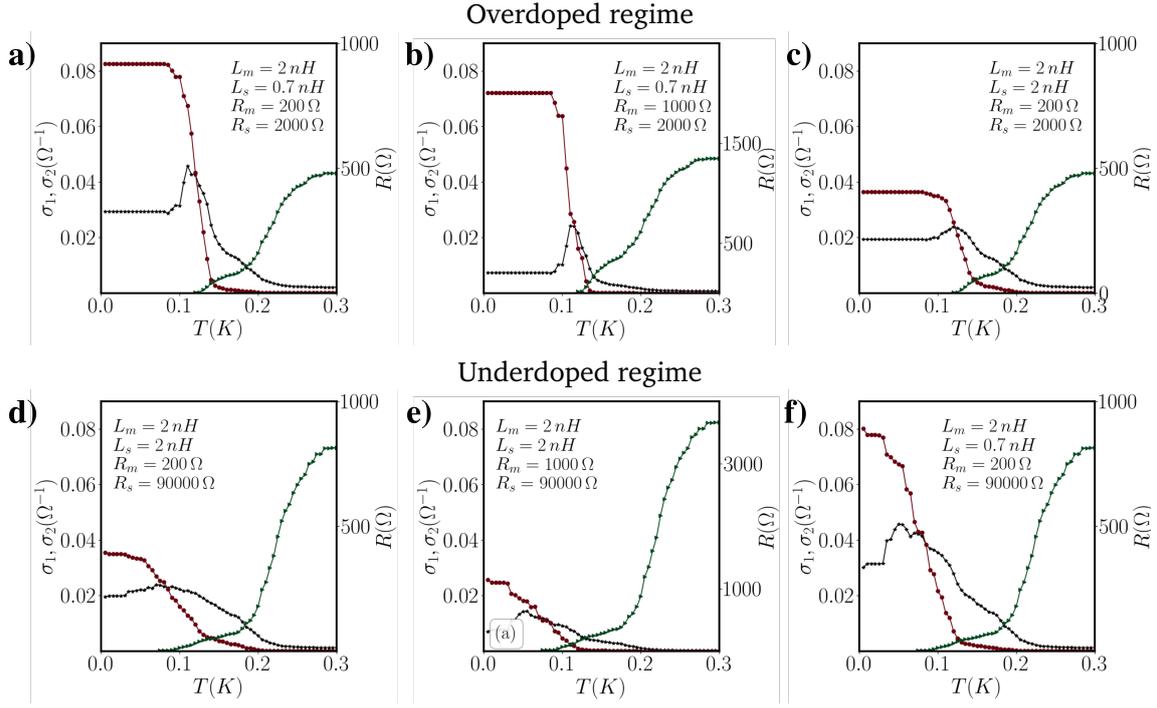
Figure 9: Temperature dependence of complex conductivity (real part in black, imaginary part in red and DC resistivity in green) and DC resistivity calculated with the RIN model using the same parameters and probability distributions of Fig. 3 (see panels c and for the OD case, panels f and g for UD). The tuning parameters are here R_m and L_s, both acting on the superfluid response, keeping $L_m = 2$nH. OD regime: $R_s = 200\,\Omega$. (a) $L_s = 0.7$ nH and $R_m = 200\,\Omega$, (b) $L_s = 0.7$ nH and $R_m = 1000\,\Omega$, (c) $L_s = 2$ nH and $R_m = 200\,\Omega$. UD regime: $R_s = 90000$

References

[1] B. Leridon, S. Caprara, J. Vanacken, V. Moshchalkov, B. Vignolle, R. Porwal, R. Budhani, A. Attanasi, M. Grilli and J. Lorenzana, *Protected superconductivity at the boundaries of charge-density-wave domains*, New Journal of Physics **22**(7), 073025 (2020).

[2] S. Caprara, M. Grilli, J. Lorenzana and B. Leridon, *Doping-dependent competition between superconductivity and polycrystalline charge density waves*, SciPost Physics **8**(1), 003 (2020).

[3] M. Spera, A. Scarfato, E. Giannini and C. Renner, *Energy-dependent spatial texturing of charge order in* $1T - Cu_x TiSe_2$, Physical Review B **99**(15), 155133 (2019).

[4] L. Li, E. O'Farrell, K. Loh, G. Eda, B. Özyilmaz and A. C. Neto, *Controlling many-body states by the electric-field effect in a two-dimensional material*, Nature **529**(7585), 185 (2016).

[5] J. Li, J. Peng, S. Zhang and G. Chen, *Anisotropic multichain nature and filamentary superconductivity in the charge density wave system* $HfTe_3$, Physical Review B **96**(17), 174510 (2017).

[6] M. Li, J. Huang, W. Guo, R. Yang, T. Hu, A. Yu, Y. Huang, M. Zhang, W. Zhang, J.-M. Zhang *et al.*, *Pressure tuning of the iron-based superconductor* $(Ca_0.73La_0.27)FeAs_2$, Physical Review B **103**(2), 024502 (2021).

[7] H. Xiao, T. Hu, A. Dioguardi, A. Shockley, J. Crocker, D. Nisson, Z. Viskadourakis, X. Tee, I. Radulov, C. Almasan *et al.*, *Evidence for filamentary superconductivity nucleated at antiphase domain walls in antiferromagnetic* $CaFe_2As_2$, Physical Review B **85**(2), 024530 (2012).

[8] H. Xiao, T. Hu, S. He, B. Shen, W. Zhang, B. Xu, K. He, J. Han, Y. Singh, H. Wen *et al.*, *Filamentary superconductivity across the phase diagram of* $Ba(Fe, Co)_2As_2$, Physical Review B **86**(6), 064521 (2012).

[9] K. Gofryk, M. Pan, C. Cantoni, B. Saparov, J. E. Mitchell and A. S. Sefat, *Local inhomogeneity and filamentary superconductivity in* Pr-*doped* $CaFe_2As_2$, Physical Review Letters **112**(4), 047005 (2014).

[10] E. W. Carlson, D. X. Yao and D. K. Campbell, *Spin waves in striped phases*, Physical Review B **70**, 064505 (2004).

[11] J. Zhao, D.-X. Yao, S. Li, T. Hong, Y. Chen, S. Chang, W. Ratcliff, J. W. Lynn, H. A. Mook, G. F. Chen, J. L. Luo, N. L. Wang *et al.*, *Low energy spin waves and magnetic interactions in* $SrFe_2As_2$, Physical Review Letters **101**, 167203 (2008).

[12] A. Shengelaya, K. Conder and K. Müller, *Signatures of filamentary superconductivity up to 94 k in tungsten oxide* $WO_{2.90}$, Journal of Superconductivity and Novel Magnetism **33**(2), 301 (2020).

[13] G. Dezi, N. Scopigno, S. Caprara and M. Grilli, *Negative electronic compressibility and nanoscale inhomogeneity in ionic-liquid gated two-dimensional superconductors*, Physical Review B **98**(21), 214507 (2018).

[14] Y. Chen, N. Pryds, J. E. Kleibeuker, G. Koster, J. Sun, E. Stamate, B. Shen, G. Rijnders and S. Linderoth, *Metallic and insulating interfaces of amorphous* $SrTiO_3$-*based oxide heterostructures*, Nano letters **11**(9), 3774 (2011).

[15] G. De Luca, A. Rubano, E. d. Gennaro, A. Khare, F. M. Granozio, U. S. di Uccio, L. Marrucci and D. Paparo, *Potential-well depth at amorphous-*LaAlO$_3$*/crystalline-*SrTiO$_3$ *interfaces measured by optical second harmonic generation*, Applied Physics Letters **104**(26), 261603 (2014).

[16] N. Scopigno, D. Bucheli, S. Caprara, J. Biscaras, N. Bergeal, J. Lesueur and M. Grilli, *Phase separation from electron confinement at oxide interfaces*, Physical Review Letters **116**(2), 026804 (2016).

[17] N. Nakagawa, H. Y. Hwang and D. A. Muller, *Why some interfaces cannot be sharp*, Nature Materials **5**(3), 204 (2006).

[18] L. Yu and A. Zunger, *A polarity-induced defect mechanism for conductivity and magnetism at polar–nonpolar oxide interfaces*, Nature Communications **5**(1), 1 (2014).

[19] S. Caprara, F. Peronaci and M. Grilli, *Intrinsic instability of electronic interfaces with strong rashba coupling*, Physical Review Letters **109**, 196401 (2012).

[20] D. Bucheli, M. Grilli, F. Peronaci, G. Seibold and S. Caprara, *Phase diagrams of voltage-gated oxide interfaces with strong Rashba coupling*, Physical Review B **89**(19), 195448 (2014).

[21] S. Caprara, M. Grilli, L. Benfatto and C. Castellani, *Effective medium theory for superconducting layers: A systematic analysis including space correlation effects*, Physical Review B **84**(1), 014514 (2011).

[22] N. Reyren, S. Thiel, A. Caviglia, L. F. Kourkoutis, G. Hammerl, C. Richter, C. W. Schneider, T. Kopp, A.-S. Rüetschi, D. Jaccard *et al.*, *Superconducting interfaces between insulating oxides*, Science **317**(5842), 1196 (2007).

[23] A. Caviglia, S. Gariglio, N. Reyren, D. Jaccard, T. Schneider, M. Gabay, S. Thiel, G. Hammerl, J. Mannhart and J.-M. Triscone, *Electric field control of the* LaAlO$_3$/SrTiO$_3$ *interface ground state*, Nature **456**(7222), 624 (2008).

[24] J. Ye, Y. J. Zhang, R. Akashi, M. S. Bahramy, R. Arita and Y. Iwasa, *Superconducting dome in a gate-tuned band insulator*, Science **338**(6111), 1193 (2012).

[25] Y. Saito, Y. Kasahara, J. Ye, Y. Iwasa and T. Nojima, *Metallic ground state in an ion-gated two-dimensional superconductor*, Science **350**(6259), 409 (2015).

[26] S. Kirkpatrick, *Percolation and conduction*, Reviews of modern physics **45**(4), 574 (1973).

[27] N. P. Breznay and A. Kapitulnik, *Particle-hole symmetry reveals failed superconductivity in the metallic phase of two-dimensional superconducting films*, Science advances **3**(9), e1700612 (2017).

[28] Y. Wang, I. Tamir, D. Shahar and N. P. Armitage, *Absence of cyclotron resonance in the anomalous metallic phase in* ino$_x$, Phys. Rev. Lett. **120**, 167002 (2018).

[29] A. Kapitulnik, S. A. Kivelson and B. Spivak, *Colloquium: anomalous metals: failed superconductors*, Reviews of Modern Physics **91**(1), 011002 (2019).

[30] V. Krivoruchko and V. Y. Tarenkov, *Percolation transitions in d-wave superconductor–half-metallic ferromagnet nanocomposites*, Low Temperature Physics **45**(5), 476 (2019).

[31] G. Venditti, J. Biscaras, S. Hurand, N. Bergeal, J. Lesueur, A. Dogra, R. C. Budhani, M. Mondal, J. Jesudasan, P. Raychaudhuri, S. Caprara and L. Benfatto, *Nonlinear $I-V$ characteristics of two-dimensional superconductors:* Berezinskii$-$Kosterlitz$-$Thouless *physics versus inhomogeneity*, Physical Review B **100**, 064506 (2019).

[32] D. Bucheli, S. Caprara and M. Grilli, *Pseudo-gap as a signature of inhomogeneous superconductivity in oxide interfaces*, Superconductor Science and Technology **28**(4), 045004 (2015).

[33] P. Popčević, D. Pelc, Y. Tang, K. Velebit, Z. Anderson, V. Nagarajan, G. Yu, M. Požek, N. Barišić and M. Greven, *Percolative nature of the direct-current paraconductivity in cuprate superconductors*, npj Quantum Materials **3**(1), 42 (2018).

[34] D. Pelc, M. Vučković, M. S. Grbić, M. Požek, G. Yu, T. Sasagawa, M. Greven and N. Barišić, *Emergence of superconductivity in the cuprates via a universal percolation process*, Nature communications **9**(1), 4327 (2018).

[35] I. F Llovo, J. Mosqueira and F. Vidal, *On the dilemma between percolation processes and fluctuating pairs as the origin of the enhanced conductivity above the superconducting transition in cuprates*, Superconductor Science and Technology (2023).

[36] G. Venditti, I. Maccari, M. Grilli and S. Caprara, *Superfluid properties of superconductors with disorder at the nanoscale:* A Random Impedance Model, Condensed Matter **5**(2), 36 (2020).

[37] G. Venditti, I. Maccari, M. Grilli and S. Caprara, *Finite-frequency dissipation in two-dimensional superconductors with disorder at the nanoscale*, Nanomaterials **11**(8), 1888 (2021).

[38] C. Carbillet, S. Caprara, M. Grilli, C. Brun, T. Cren, F. Debontridder, B. Vignolle, W. Tabis, D. Demaille, L. Largeau, K. Ilin, M. Siegel *et al.*, *Intrinsic instability of electronic interfaces with strong rashba coupling*, Physical Review B **93**, 144509 (2016).

[39] P. Raychaudhuri and S. Dutta, *Phase fluctuations in conventional superconductors*, Journal of Physics: Condensed Matter **34**(8), 083001 (2021).

[40] V. L. Berezinsky, *Destruction of long-range order in one-dimensional and two-dimensional systems having a continuous symmetry group* I. *Classical systems*, Soviet Physics JETP **32**(3), 907 (1972).

[41] J. M. Kosterlitz and D. J. Thouless, *Ordering, metastability and phase transitions in two-dimensional systems*, Journal of Physics C: Solid State Physics **6**(7), 1181 (1973).

[42] J. Kosterlitz, *The critical properties of the two-dimensional XY model*, Journal of Physics C: Solid State Physics **7**(6), 1046 (1974).

[43] A. B. Harris, *Effect of random defects on the critical behaviour of ising models*, Journal of Physics C: Solid State Physics **7**(9), 1671 (1974).

[44] I. Maccari, L. Benfatto and C. Castellani, *Disordered* XY *model: Effective medium theory and beyond*, Physical Review B **99**(10), 104509 (2019).

[45] I. Maccari, L. Benfatto and C. Castellani, *Broadening of the berezinskii-Kosterlitz-thouless transition by correlated disorder*, Physical Review B **96**, 060508 (2017).

[46] I. Maccari, L. Benfatto and C. Castellani, *The* BKT *universality class in the presence of correlated disorder*, Condensed Matter **3**(1), 8 (2018).

[47] M. Tinkham, *Introduction to superconductivity*, Courier Corporation (2004).

[48] D. Bucheli, S. Caprara, C. Castellani and M. Grilli, *Metal–superconductor transition in low-dimensional superconducting clusters embedded in two-dimensional electron systems*, New Journal of Physics **15**(2), 023014 (2013).

[49] S. Caprara, J. Biscaras, N. Bergeal, D. Bucheli, S. Hurand, C. Feuillet-Palma, A. Rastogi, R. Budhani, J. Lesueur and M. Grilli, *Multiband superconductivity and nanoscale inhomogeneity at oxide interfaces*, Physical Review B **88**(2), 020504 (2013).

[50] S. Caprara, D. Bucheli, N. Scopigno, N. Bergeal, J. Biscaras, S. Hurand, J. Lesueur and M. Grilli, *Inhomogeneous multi carrier superconductivity at* $LaXO_3/SrTiO_3$ *(X = Al or Ti) oxide interfaces*, Superconductor Science and Technology **28**(1), 014002 (2014).

[51] C. Richter, H. Boschker, W. Dietsche, E. Fillis-Tsirakis, R. Jany, F. Loder, L. F. Kourkoutis, D. A. Muller, J. R. Kirtley, C. W. Schneider *et al.*, *Interface superconductor with gap behaviour like a high-temperature superconductor*, Nature **502**(7472), 528 (2013).

[52] M. Huang, F. Bi, S. Ryu, C.-B. Eom, P. Irvin and J. Levy, *Direct imaging of laalo3/srtio3 nanostructures using piezoresponse force microscopy*, APL Materials **1**(5), 052110 (2013).

[53] G. E. D. K. Prawiroatmodjo, F. Trier, D. V. Christensen, Y. Chen, N. Pryds and T. S. Jespersen, *Evidence of weak superconductivity at the room-temperature grown* $LaXO_3/SrTiO_3$ *interface*, Physical Review B **93**, 184504 (2016).

[54] J. A. Bert, K. C. Nowack, B. Kalisky, H. Noad, J. R. Kirtley, C. Bell, H. K. Sato, M. Hosoda, Y. Hikita, H. Y. Hwang *et al.*, *Gate-tuned superfluid density at the superconducting* $LaAlO_3/SrTiO_3$ *interface*, Physical Review B **86**(6), 060503 (2012).

[55] J. Biscaras, N. Bergeal, S. Hurand, C. Feuillet-Palma, A. Rastogi, R. Budhani, M. Grilli, S. Caprara and J. Lesueur, *Multiple quantum criticality in a two-dimensional superconductor*, Nature Materials **12**(6), 542 (2013).

[56] B. Kalisky, E. M. Spanton, H. Noad, J. R. Kirtley, K. C. Nowack, C. Bell, H. K. Sato, M. Hosoda, Y. Xie, Y. Hikita *et al.*, *Locally enhanced conductivity due to the tetragonal domain structure in* $LaAlO_3/SrTiO_3$ *heterointerfaces*, Nature Materials **12**(12), 1091 (2013).

[57] M. Honig, J. A. Sulpizio, J. Drori, A. Joshua, E. Zeldov and S. Ilani, *Local electrostatic imaging of striped domain order in* $LaAlO_3/SrTiO_3$, Nature Materials **12**(12), 1112 (2013).

[58] G. Singh, A. Jouan, L. Benfatto, F. Couëdo, P. Kumar, A. Dogra, R. Budhani, S. Caprara, M. Grilli, E. Lesne *et al.*, *Competition between electron pairing and phase coherence in superconducting interfaces*, Nature Communications **9**(1), 1 (2018).

[59] R. Ganguly, D. Chaudhuri, P. Raychaudhuri and L. Benfatto, *Slowing down of vortex motion at the berezinskii-kosterlitz-thouless transition in ultrathin nbn films*, Physical Review B **91**(5), 054514 (2015).

[60] M. V. Mazziotti, N. Scopigno, M. Grilli and S. Caprara, *Majorana fermions in one-dimensional structures at* $LaAlO_3/SrTiO_3$ *oxide interfaces*, Condensed Matter **3**(4), 37 (2018).

[61] W. H. Press, *Numerical recipes 3rd edition: The art of scientific computing*, Cambridge university press (2007).

[62] G. Singh, A. Jouan, G. Herranz, M. Scigaj, F. Sánchez, L. Benfatto, S. Caprara, M. Grilli, G. Saiz, F. Couëdo *et al.*, *Gap suppression at a Lifshitz transition in a multi-condensate superconductor*, Nature Materials **18**(9), 948 (2019).

[63] S. Mallik, G. Ménard, G. Saïz, H. Witt, J. Lesueur, A. Gloter, L. Benfatto, M. Bibes and N. Bergeal, *Superfluid stiffness of a* $KTaO_3$*-based two-dimensional electron gas*, Nature Communications **13**(1), 4625 (2022).

[64] J. Biscaras, N. Bergeal, S. Hurand, C. Grossetête, A. Rastogi, R. Budhani, D. LeBoeuf, C. Proust and J. Lesueur, *Two-dimensional superconducting phase in* $LaAlO_3/SrTiO_3$ *heterostructures induced by high-mobility carrier doping*, Physical review letters **108**(24), 247004 (2012).

[65] Z. Wang, Z. Zhong, X. Hao, S. Gerhold, B. Stöger, M. Schmid, J. Sánchez-Barriga, A. Varykhalov, C. Franchini, K. Held *et al.*, *Anisotropic two-dimensional electron gas at* $SrTiO_3$ *(110)*, Proceedings of the National Academy of Sciences **111**(11), 3933 (2014).